Imaging Electron Wave Functions Inside Open Quantum Rings

F. Martins,[1] B. Hackens,[1,2,*] M. G. Pala,[3,†] T. Ouisse,[1,‡] H. Sellier,[1] X. Wallart,[4] S. Bollaert,[4] A. Cappy,[4] J. Chevrier,[1] V. Bayot,[2] and S. Huant[1]

[1]*Institut Néel, CNRS and Université Joseph Fourier, BP 166, 38042 Grenoble cedex 9, France*
[2]*CERMIN, DICE Lab, Université Catholique de Louvain, B-1348 Louvain-la-Neuve, Belgium*
[3]*IMEP-MINATEC (UMR CNRS/INPG/UJF 5130), BP 257, 38016 Grenoble, France*
[4]*IEMN, Centre National de la Recherche Scientifique, UMR 8520, BP 60069, Avenue Poincaré, 59652 Villeneuve d'Ascq, France*

(Received 21 May 2007; published 28 September 2007)

Combining scanning gate microscopy (SGM) experiments and simulations, we demonstrate low temperature imaging of the electron probability density $|\Psi|^2(x, y)$ in embedded mesoscopic quantum rings. The tip-induced conductance modulations share the same temperature dependence as the Aharonov-Bohm effect, indicating that they originate from electron wave function interferences. Simulations of both $|\Psi|^2(x, y)$ and SGM conductance maps reproduce the main experimental observations and link fringes in SGM images to $|\Psi|^2(x, y)$.

DOI: 10.1103/PhysRevLett.99.136807 PACS numbers: 85.35.Ds, 03.65.Yz, 73.21.La, 73.23.Ad

Thanks to the scanning tunnelling microscope (STM), remarkable precision has been achieved in the local scale imaging of surface electron systems. Only a few years after the STM invention, electron interferences could be visualized in real space inside artificially confined surface structures, the ''quantum corrals'' [1]. However, since they rely on the measurement of a current between a tip and the sample, STM techniques are useless when the system of interest is buried under an insulating layer, as in two-dimensional electron gases (2DEGs) confined in semiconductor heterostructures. To circumvent the obstacle, a new method was developed: the Scanning Gate Microscopy (SGM). SGM consists of mapping the conductance of the system as the polarized tip, acting as a flying nanogate, scans at a constant distance above the 2DEG. SGM gave many valuable insights into the physics of quantum point contacts (QPCs) [2], Coulomb-blockaded quantum dots [3], magnetic focusing [4], carbon nanotubes [5], open billiards [6], and 2DEGs in the quantum Hall regime [7].

In some cases, the mechanism of SGM image formation is readily understandable. For example, in the vicinity of a QPC [2], coherent electron flow is imaged due to multiple reflections and interferences of electrons bouncing between the QPC and the tip-induced depleted region. In comparison, the situation seems more complex when the tip scans directly over an open mesoscopic billiard [6]: the tip perturbation extends over the whole system of interest, so that *all* semiclassical trajectories are modified. The mechanisms that link conductance maps to the properties of unperturbed electrons still need to be clarified. Recently, we showed that SGM images in the vicinity of a quantum ring (QR) allow direct observation of isophase lines for electrons in an electrostatic Aharonov-Bohm (AB) experiment [8].

In this Letter, we discuss SGM images obtained as the tip scans directly over coherent QRs. Experimentally, we find that the amplitude of conductance modulations shares a common temperature dependence with the Aharonov-Bohm effect, a direct evidence that SGM probes the quantum nature of electrons. On the other hand, we perform quantum mechanical simulations of SGM experiments. First, the amplitude of conductance fringes is found to evolve linearly at low perturbation amplitude, both in experiments and simulations. Second, we observe a direct correspondence between simulated SGM data and simulations of the electron probability density $|\Psi|^2(x, y, E_F)$. We deduce that, in this linear regime, SGM reliably maps $|\Psi|^2(x, y, E_F)$ in coherent QRs.

We fabricated two QRs, samples $R1$ and $R2$, from an InGaAs/InAlAs heterostructure using electron beam lithography and wet etching [9]. The 2DEG is located 25 nm below the surface, and its low temperature (T) electron density and mobility are 2×10^{16} m^{-2} and 10 m^2/V s, respectively. Figure 1(a) shows an electron micrograph of $R2$ and a scheme of our experimental setup. The ring inner and outer (lithographic) diameters are 240 and 580 nm, respectively (210 and 600 nm in $R1$). At $T = 4.2$ K and after illumination, the conductances G of $R1$ and $R2$ are 5.9 and $2.6 \times 2e^2/h$, respectively; i.e., several quantum modes are populated in the device openings.

Figure 1(b) plots the low-T conductance ΔG of $R2$ as a function of the magnetic field B after subtraction of a slowly varying background. Periodic oscillations of ΔG vs B are clearly visible at 3.8 and 28.0 K. They are the signature of phase shifts between electron wave functions transmitted through both arms of the QR, i.e., the Aharonov-Bohm effect. The damping of AB oscillations observed as T increases [Fig. 1(b)] is related to the decay of the electron coherence time τ_ϕ. Nevertheless, the persistence of AB oscillations guarantees that transport is at least partially coherent up to $T \sim 30$ K.

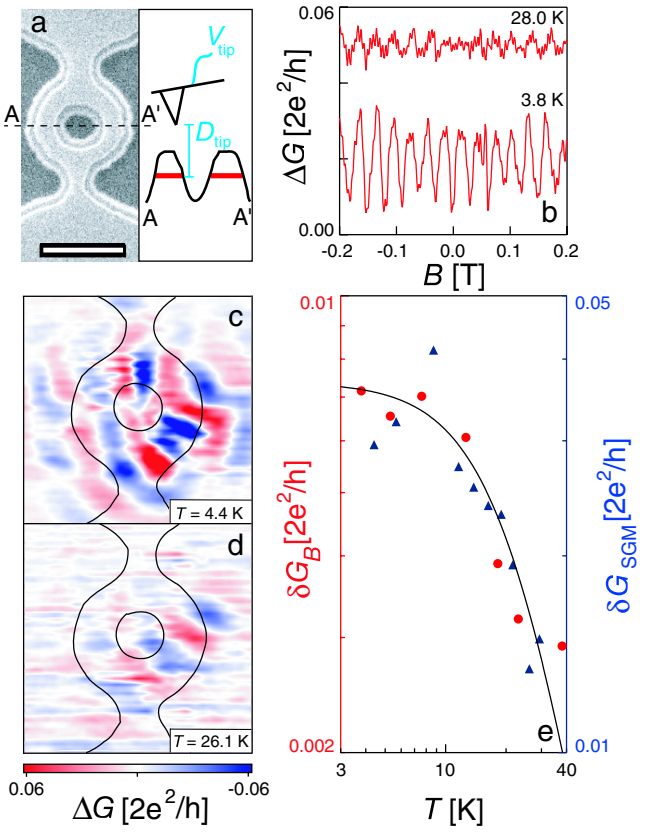

FIG. 1 (color online). (a) Left : electron micrograph of sample $R2$. The white bar represents 500 nm. Right : Scheme of the SGM experiment (side view). The curve represents the profile of the quantum ring along A-A', the bold straight lines represent the 2DEG. (b) ΔG vs B at 3.8 and 28.0 K in $R2$. (c-d) $\Delta G(x, y)$ maps measured on sample $R2$ at $V_{tip} = 0$ V, $D_{tip} = 50$ nm, $B = 0$ T and $T = 4.4$ and 26.1 K, respectively. (e) Circles: δG_B vs T (left axis); Triangles: δG_{SGM} vs T (right axis). The curve is a guide to the eye.

We then perform scanning gate microscopy in this coherent regime of transport. Figure 1(a) illustrates our imaging technique: a voltage V_{tip} is applied on the tip, which scans along a plane parallel to the 2DEG at a typical tip-2DEG distance $D_{tip} = 50$ nm. Because of the capacitive tip-2DEG coupling, a local perturbation is generated in the potential experienced by electrons within the QR, which, in turn, alters their transmission through the device. By recording the QR conductance as the tip is scanned over the QR and its vicinity, we build a conductance map $G(x, y)$ that reflects changes in electron transmission.

The measured G maps reveal a rich pattern of conductance fringes superimposed on a broad and slowly varying background, insensitive to temperature and to B [8], indicating that it is not related to quantum transport. We remove the background contribution by high-pass filtering the raw G maps [8]. Figures 1(c) and 1(d) show such filtered ΔG maps measured on $R2$ at $T = 4.4$ and 26.1 K. These SGM images are not symmetric, most probably due to unavoidable asymmetry in the QR geometry. Moreover, ΔG fringes are not limited to the area of the QR: even when the tip scans away from the QR, it perturbs the QR potential and affects its conductance. In an earlier work [8], we showed that concentric ΔG fringes observed outside the QR area originate from the electrostatic AB effect, and correspond to isophase lines for electrons. Here, we focus on the ΔG fringes measured when the tip scans directly over the QR.

In Figs. 1(c) and 1(d), we note a decay of ΔG fringe amplitude with increasing T, but the fringes pattern remains essentially unchanged. If we define δG_{SGM}, the standard deviations of the filtered conductance maps, calculated on a 400-nm diameter circle centered on the QR, and δG_B, the standard deviation of AB oscillations in G vs B, we can compare the T-dependences of SGM images and AB effect [Fig. 1(e)]. δG_B and δG_{SGM} clearly follow the same T-dependence: a strong decay above $T \sim 10$ K, and a saturation at lower T, consistent with the intrinsic saturation of τ_ϕ previously reported in similar confined systems [10]. This suggests that the AB effect and the central pattern of fringes in ΔG maps are intimately related and find a common origin in electron wave functions interferences. The question is then: do ΔG maps bear spatial informations on electron wave functions?

To investigate further on the SGM imaging mechanism, we need to examine the influence of a key ingredient: the perturbing potential [11]. Experimentally, a way to control this parameter is to change the tip voltage. Figures 2(a)–2(c) show a sequence of ΔG maps measured at $V_{tip} = 0.5$, 2.5, and 3.5 V on $R1$. Clearly, the amplitude of conductance fringes increases with V_{tip}. Furthermore, we note a strong similarity between the central patterns in successive ΔG maps. This contrasts with aperiodic conductance fluctua-

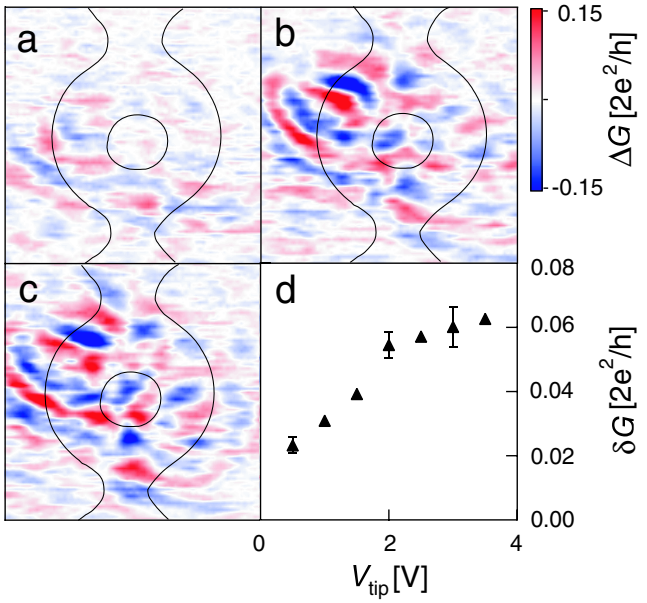

FIG. 2 (color online). (a–c) $\Delta G(x, y)$ measured on $R1$ at $D_{tip} = 50$ nm, $T = 4.2$ K, $B = 2$ T, and $V_{tip} = 0.5$, 2.5, and 3.5 V, respectively. (d) δG_{SGM} vs V_{tip} in $R1$.

tions observed in most mesoscopic systems when changing gate voltages [6,12], as well as with the concentric fringes observed on the same QR sample, but away from its central region [8]. Figure 2(d), showing the fringe amplitude δG_{SGM} vs V_{tip}, confirms the absence of fluctuations and the smooth evolution of fringes amplitude: δG_{SGM} increases linearly up to $V_{\mathrm{tip}} = 2$ V, with a somewhat weaker dependence at larger V_{tip}.

This striking behavior is now addressed by quantum mechanical simulations where we compute device conductance and local density of states (LDOS) at the Fermi energy $|\Psi|^2(x, y, E_F)$ in the scattering matrix formalism and using the Landauer-Büttiker formula, with the same method as in Ref. [13]. The geometry of the simulated QR is that of sample $R1$, taking the depletion length at device edges into account (~35 nm); i.e., the inner and outer radii or the ring are 140 and 265 nm, respectively, and the width of the ring's openings is 120 nm. The ring is subdivided into slices perpendicular to x-axis (propagating direction) between both openings in the QR. The Schrödinger equation is numerically solved in each slice, and, by imposing the continuity of the wave function and of the current density at the interface, the scattering matrix between two slices is obtained as prescribed in Ref. [14]. The overall scattering matrix is computed by composing the matrices of all slices.

When E_F is varied, both the configuration of resonant states within the QR and their coupling to the reservoirs change [15]. As a consequence, the calculated conductance G exhibits fluctuations as a function of E_F, one of the hallmarks of transport in open mesoscopic systems. This is illustrated in Fig. 3(a), showing the calculated G as a function of E_F around the measured E_F^{2DEG} value in the unpatterned heterostructure. Figures 3(b)–3(d) show typical patterns of $|\Psi|^2(x, y, E_F)$ in our QR, for $E_F = 104.6$, 109.5, and 101.0 meV, respectively. Small-scale concentric oscillations are visible within the whole QR area in Figs. 3(b)–3(d), whose characteristic spatial periodicity is related to the Fermi wavelength λ_F. On a scale larger than λ_F, $|\Psi|^2(x, y, E_F)$ is rather homogeneous in Figs. 3(b) and 3(c), while it exhibits four strong radial fringes in Fig. 3(d).

In analogy with the experiment, we included in our simulation a moving perturbation potential mimicking the tip effect and then calculated the conductance of the QR for each position of the perturbation. Figure 3(e) shows such a simulated conductance map $G(x, y)$, obtained for $E_F = 101$ meV, using the Gaussian potential $V(x, y) = V_m \exp\{-[\frac{(x-x_0)^2+(y-y_0)^2}{2*\sigma^2}]\}$ as the moving perturbation [16], with $V_m = E_F/200$, $\sigma = 5$ nm, and (x_0, y_0) the local position of the tip. Most importantly, a careful examination of Figs. 3(d) and 3(e) reveals that all the features visible in the simulated $|\Psi|^2(x, y, E_F)$ are also visible in the calculated G map. This striking correspondence reveals that SGM can in principle be used to map the unperturbed electron probability density [17].

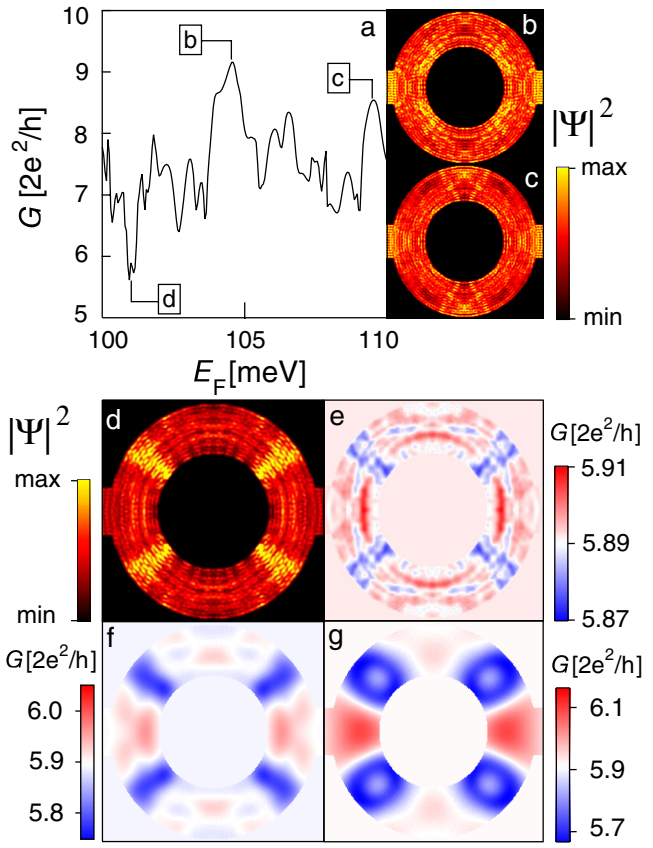

FIG. 3 (color online). (a) Calculated G vs E_F in a QR with inner and outer radii of 140 and 265 nm. (b–d) Electron probability density $|\Psi|^2(x, y, E_F)$ in a QR at $E_F = 104.6$, 109.5, and 101 meV, respectively. (e–g) Simulated $G(x, y)$ for $E_F = 101$ meV, $V_m = E_F/200$, and $\sigma = 5$, 20, and 40 nm, respectively.

Enlarging now the width of the perturbing potential causes the smallest SGM features to disappear [Figs. 3(f) and 3(g)]. As σ overcomes λ_F, concentric fringes completely vanish. Nevertheless, at the scale of radial fringes, the correspondence between $G(x, y)$ and $|\Psi|^2(x, y, E_F)$ is maintained [Fig. 3(f)] until $\sigma \gtrsim 40$ nm where the aspect of the four radial fringes changes [Fig. 3(g)]. Most importantly, the size of the smallest features in the simulated G maps is roughly correlated to σ. Based on Figs. 2(a)–2(c), this allows us to infer a lower bound for $\sigma \sim 25$ nm.

To come closer to a complete description of our experiments, we now examine the effect of the perturbation amplitude. As we increase V_m, keeping $\sigma = 20$ nm, we observe that the SGM fingerprint remains qualitatively independent of V_m, and that its amplitude increases linearly with V_m [Figs. 4(a)–4(c)], a behavior consistent with the observations related in Figs. 2(a)–2(c). Above $V_m \sim 0.8$ meV, qualitative changes in the SGM pattern appear together with a deviation from the linear evolution of δG_{SGM} vs V_m [Fig. 4(c)], a value for which differences between $G(x, y)$ and $|\Psi|^2(x, y, E_F)$ start to emerge. Figure 4(d) also shows that the evolution of δG_{SGM} vs

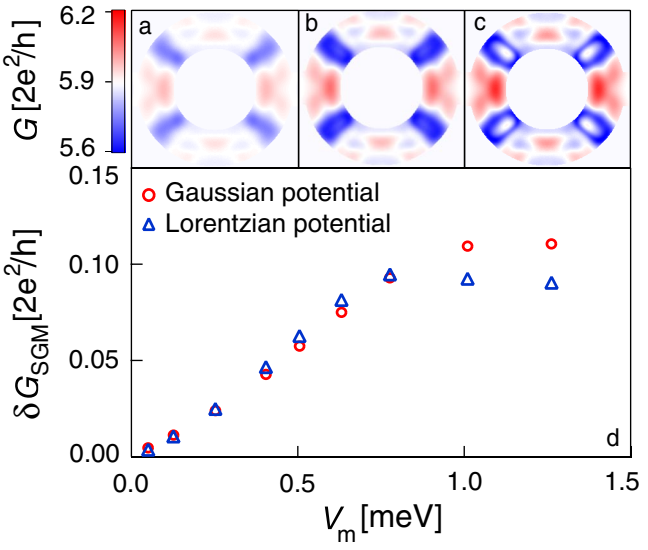

FIG. 4 (color online). (a–c) Simulated G maps, calculated for $E_F = 101$ meV, $\sigma = 20$ nm, and $V_m = 0.5$, 1.0, and 1.5 meV, respectively. (d) Fringe amplitude δG_{SGM} on simulated G maps as a function of V_m, with $\sigma = 20$ nm.

V_m is weakly affected by the exact shape of the perturbation, e.g., Lorentzian or Gaussian. The consistency between the simulated behavior of δG_{SGM} vs V_m and the experimental data in Fig. 2(d) leads us to conclude that, at low V_{tip} (below $\sim$2 V), the central part of our SGM maps directly reveals the main structure of $|\Psi|^2(x, y, E_F)$ in our quantum rings. This means that we can attribute the pattern of conductance fringes in Figs. 2(a)–2(d) to $|\Psi|^2(x, y, E_F)$ of electrons in the quantum ring. Furthermore, simulations of $|\Psi|^2(x, y, E_F)$ in asymmetric quantum rings yield asymmetric structures [18], which gives us an explanation for the asymmetry observed in the experimental ΔG maps.

In summary, we observed a pattern of fringes in conductance maps obtained by scanning gate microscopy on quantum rings. Using quantum mechanical simulations of the electron probability density, including the perturbing potential of the tip, we could reproduce the main experimental features and demonstrate the relationship between conductance maps and electron probability density maps. Hence, one can view SGM as the analog of STM for imaging the electronic LDOS in open mesoscopic systems buried under an insulating layer or the counterpart of the near-field scanning optical microscope that images the photonic LDOS in confined nanostructures [19].

F. M. is funded by FCT (Portugal) and B. H. by the EU (Marie Curie IEF) and FNRS. This work has been supported by the Communauté Française de Belgique (Actions de Recherche Concertées), by FRFC Grant No. 2.4502.05, by the Belgian Science Policy (Interuniversity Attraction Pole Program PAI), by the Action Concertée Nanoscience (French Ministry for Education and Research), and by the Institut de Physique de la Matière Condensée, Grenoble. F. M. and B. H. contributed equally to this work.

*benoit.hackens@uclouvain.be
†pala@minatec.inpg.fr
‡thierry.ouisse@grenoble.cnrs.fr

[1] M. F. Crommie, C. P. Lutz, and D. M. Eigler, Science **262**, 218 (1993).
[2] M. A. Topinka, B. J. LeRoy, S. E. J. Shaw, E. J. Heller, R. M. Westervelt, K. D. Maranowski, and A. C. Gossard, Science **289**, 2323 (2000); M. A. Topinka, B. J. LeRoy, R. M. Westervelt, S. E. J. Shaw, R. Fleischmann, E. J. Heller, K. D. Maranowski, and A. C. Gossard, Nature (London) **410**, 183 (2001); N. Aoki, C. R. Da Cunha, R. Akis, D. K. Ferry, and Y. Ochiai, Appl. Phys. Lett. **87**, 223501 (2005).
[3] A. Pioda, S. Kicin, T. Ihn, M. Sigrist, A. Fuhrer, K. Ensslin, A. Weichselbaum, S. E. Ulloa, M. Reinwald, and W. Wegscheider, Phys. Rev. Lett. **93**, 216801 (2004); P. Fallahi, A. C. Bleszynski, R. M. Westervelt, J. Huang, J. D. Walls, E. J. Heller, M. Hanson, and A. C. Gossard, Nano Lett. **5**, 223 (2005).
[4] R. Crook, C. G. Smith, M. Y. Simmons, and D. A. Ritchie, Phys. Rev. B **62**, 5174 (2000); K. E. Aidala, R. E. Parrott, T. Kramer, E. J. Heller, R. M. Westervelt, M. P. Hanson, and A. C. Gossard, Nature Phys. **3**, 464 (2007).
[5] A. Bachtold, M. S. Fuhrer, S. Plyasunov, M. Forero, E. H. Anderson, A. Zettl, and P. L. McEuen, Phys. Rev. Lett. **84**, 6082 (2000).
[6] R. Crook, C. G. Smith, A. C. Graham, I. Farrer, H. E. Beere, and D. A. Ritchie, Phys. Rev. Lett. **91**, 246803 (2003).
[7] G. Finkelstein, P. I. Glicofridis, R. C. Ashoori, and M. Shayegan, Science **289**, 90 (2000).
[8] B. Hackens, F. Martins, T. Ouisse, H. Sellier, S. Bollaert, X. Wallart, A. Cappy, J. Chevrier, V. Bayot, and S. Huant, Nature Phys. **2**, 826 (2006).
[9] Data from a first set of measurements on $R1$ were presented in Ref. [8]. Here, we present new data on $R1$, focusing on the central part of the QR.
[10] B. Hackens, S. Faniel, C. Gustin, X. Wallart, S. Bollaert, A. Cappy, and V. Bayot, Phys. Rev. Lett. **94**, 146802 (2005).
[11] A. E. Gildemeister *et al.*, Phys. Rev. B **75**, 195338 (2007).
[12] B. Krafft, A. Forster, A. van der Hart, and T. Schapers, Physica E (Amsterdam) **9**, 635 (2001).
[13] M. G. Pala and G. Iannaccone, Phys. Rev. B **69**, 235304 (2004).
[14] M. Macucci and K. Hess, Phys. Rev. B **46**, 15357 (1992).
[15] R. Akis, D. K. Ferry, and J. P. Bird, Phys. Rev. Lett. **79**, 123 (1997).
[16] In SGM measurements on isolated quantum dots [11], the shape of the tip potential was found to be Lorentzian. In our simulated G maps, we did not observe significant differences between Gaussian and Lorentzian perturbing potential of comparable amplitude and lateral extension.
[17] In the case of a repulsive potential and for $E_F = 101$ meV (as in our simulations), a minimum is observed in G maps for a maximum in $|\Psi|^2$. For an attractive potential, a maximum in $|\Psi|^2$ corresponds to a maximum in G maps.
[18] M. G. Pala *et al.* (to be published).
[19] G. Colas des Francs, C. Girard, J.-C. Weeber, C. Chicane, T. David, A. Dereux, and D. Peyrade, Phys. Rev. Lett. **86**, 4950 (2001).